Dynamic simulation and monitoring of a non-contacting flexibly mounted rotor mechanical face seal

M Zou, J Dayan and **I Green***
The George W. Woodruff School of Mechanical Engineering, Georgia Institute of Technology, Atlanta, Georgia, USA

Abstract: Mechanical face seal rotor dynamics is investigated through both simulation and real-time monitoring of a non-contacting flexibly mounted rotor (FMR) mechanical face seal in a seal test rig. Dynamic simulation is performed to investigate the seal rotor angular response to the stator misalignment, the stator angle, the initial rotor misalignment and clearance. Rotor angular response orbit is introduced and is able to characterize the rotor dynamic response. A real-time monitoring system is constructed in the test rig to monitor the instantaneous dynamic behaviour of the seal rotor, including its angular response, precession angle and angular response orbit. Experimental results agree qualitatively well with those of the dynamic simulation. Potential applications of the monitoring system for detecting seal face contact and for seal control are stated.

Keywords: non-contacting face seal, mechanical seal monitoring, face seal dynamics, dynamic simulation

NOTATION

D_f	fluid film angular damping coefficient
D_{f33}	fluid film axial damping coefficient
D_s	support angular damping coefficient
D_{s33}	support axial damping coefficient
F_{air}	air force acting on the rotor
I_p	rotor polar moment of inertia
I_t	rotor transverse moment of inertia
K_f	fluid film angular stiffness coefficient
K_{f33}	fluid film axial stiffness coefficient
K_s	support angular stiffness coefficient
K_{s33}	support axial stiffness coefficient
m	rotor mass
t	time
Z	seal axial displacement from the equilibrium position
γ_{ri}	initial rotor misalignment
γ_s	fixed stator misalignment
γ_ξ, γ_η	rotor tilt in the inertial system $\xi\eta\zeta$
ψ_s	stator angle, i.e. the angle between the X_s and ξ axes
ω	shaft rotating speed

The MS was received on 25 February 1999 and was accepted after revision for publication on 6 September 1999.
** Corresponding author: The GWW School of Mechanical Engineering, Georgia Institute of Technology, Atlanta, GA 30332-0405, USA.*

1 INTRODUCTION

Mechanical face seals are typically used for liquid/gas sealing, such as in centrifugal pumps, compressors and powered vessels. Two seal types have evolved in mechanical seal design: contacting and non-contacting mechanical face seals. Contacting seals are designed to operate with face contact to minimize leakage at the cost of friction and wear of seal faces. Non-contacting seals are designed to operate with some face separation to reduce frictional heat generation and wear at the cost of some leakage. Despite their wide application in industry, non-contacting seals generally have unpredictable life, and their premature and random failures are not uncommon. One of the causes of seal failure is contact between the faces. The study of seal dynamics is very important for a full understanding of face non-contacting operation and face separation. It has been the subject of extensive work during the past three decades [**1**]. Different seal configurations have been studied, including flexibly mounted stator (FMS), flexibly mounted rotor (FMR), and flexibly mounted stator and rotor mechanical seals (FMSR). The dynamics of a non-contacting FMR seal, such as the seal in the test rig used in this study and depicted in Fig. 1, was studied by Green [**2**–**4**]. The linearized fluid film dynamic coefficients were first derived [**2**], and then the equations of motion of the seal rotor were constructed and stability was investigated [**3**]. Finally, the steady state response of the rotor was solved in a closed form [**4**]. These works provide important theoretical insight into rotor

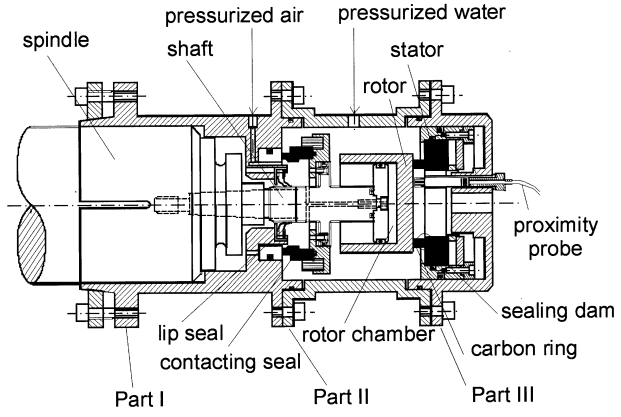

Fig. 1 Schematic of the FMR non-contacting mechanical seal assembly

dynamics of the non-contacting FMR mechanical face seal and could further lead to better seal design, condition monitoring and face contact control.

Condition monitoring of mechanical face seals has been the subject of several research efforts. The acoustic emission (AE) method for monitoring seal failures was pioneered by Bloch in reference [**5**]. A similar attempt was made by Kataoka *et al.* [**6**]. However, there are still many technical challenges to be solved before the AE method can be considered as a reliable method for predicting failure in mechanical seals. One of the challenges is to determine what information can be obtained from a measured AE and whether or not the information obtained can be used to detect and predict failures in seals [**6**]. Background noise from the rotating machinery is another major obstacle.

Because seal failure is often characterized by worn faces caused by rubbing contact between the rotor and the stator, contact detection offers an alternative approach for seal condition monitoring. To date, only a few studies have been performed in seal contact detection. Kennedy and Grim [**7**] built a contact probe/thermocouple to study the characteristics of small patches of solid-to-solid contact at the sealing interface of mechanical face seals during operation. The contact probe used in Kennedy's research required a fine wire to be implanted in the seal. Lee and Green [**8**] detected contact by observing the presence of higher-harmonic oscillations (HHO) in proximity probe signals in a non-contacting FMR mechanical seal test rig; yet these HHO were discovered in an off-line data analysis.

The objective of this research is to devise a real-time condition monitoring system for the dynamic behaviour of a non-contacting FMR mechanical face seal. Numerical simulation is performed first to establish the foundation for understanding the experimental results as detected by the monitoring system. The dynamic simulation and the real-time monitoring system are discussed in detail in the following sections. Finally, comparison is made between the simulation and experimental results.

2 SEAL DYNAMIC SIMULATIONS

2.1 Seal dynamic response

Several coordinate systems are used to describe the non-contacting FMR mechanical face seals (see Figs 2 and 3 in reference [**4**]). Detailed descriptions of these coordinate systems and notation can be found in reference [**4**].

The non-contacting FMR has three degrees of freedom: one axial translation along the shaft axis and two angular rotations about its two inertial axes in a plane that is perpendicular to the shaft axis. The linearized equation of motion for the seal rotor about an equilibrium position is [**3**]

$$m\ddot{Z} + (D_{s33} + D_{f33})\dot{Z} + (K_{s33} + K_{f33})Z = F_{air} \tag{1}$$

$$I_t\ddot{\gamma}_\xi + I_p\omega\dot{\gamma}_\eta + (D_s + D_f)\dot{\gamma}_\xi + (D_s + \tfrac{1}{2}D_f)\omega\gamma_\eta + (K_s + K_f)\gamma_\xi = \gamma_s(K_f \cos \psi_s + \tfrac{1}{2}D_f\omega \sin \psi_s) + K_s\gamma_{ri} \cos \omega t \tag{2}$$

$$I_t\ddot{\gamma}_\eta - I_p\omega\dot{\gamma}_\xi + (D_s + D_f)\dot{\gamma}_\eta - (D_s + \tfrac{1}{2}D_f)\omega\gamma_\xi + (K_s + K_f)\gamma_\eta = \gamma_s(K_f \sin \psi_s - \tfrac{1}{2}D_f\omega \cos \psi_s) + K_s\gamma_{ri} \sin \omega t \tag{3}$$

In equation (1), F_{air} is the axial force generated by the pressurized air in the rotor chamber of the studied seal (see details in the test rig description section). Equation (1) represents the axial degree of freedom. For a constant F_{air}, the seal clearance is determined by the balance between closing and opening forces that act on the FMR. In this case, equation (1) is decoupled from the angular degrees of freedom whose equations of motion are represented in equations (2) and (3). In cases where F_{air} varies in time (in this test rig, F_{air} is designed to change the closing force acting on the rotor and thus control the clearance), the clearance changes as well. In these cases, equations (2) and (3) are no longer decoupled from equation (1), as the clearance affects all rotor dynamic coefficients, axial and angular alike. The force generated by the air pressure in the rotor chamber, F_{air}, the stator misalignment, γ_s, and initial rotor misalignment, γ_{ri}, act as forcing functions to the seal dynamic system.

Because the clearance, C, between the rotor and the stator is very small, the rotor angular response, γ_r, and stator misalignment, γ_s, are also very small. Such small angles can be treated mathematically as tilt vectors. A vector diagram of the seal tilts and angles is shown in Fig. 2. The total rotor angular response, γ_r, is a vector sum (superposition) of two responses, γ_{rs} and γ_{rI}; γ_{rs} is the rotor response to γ_s and γ_{rI} is the rotor response to

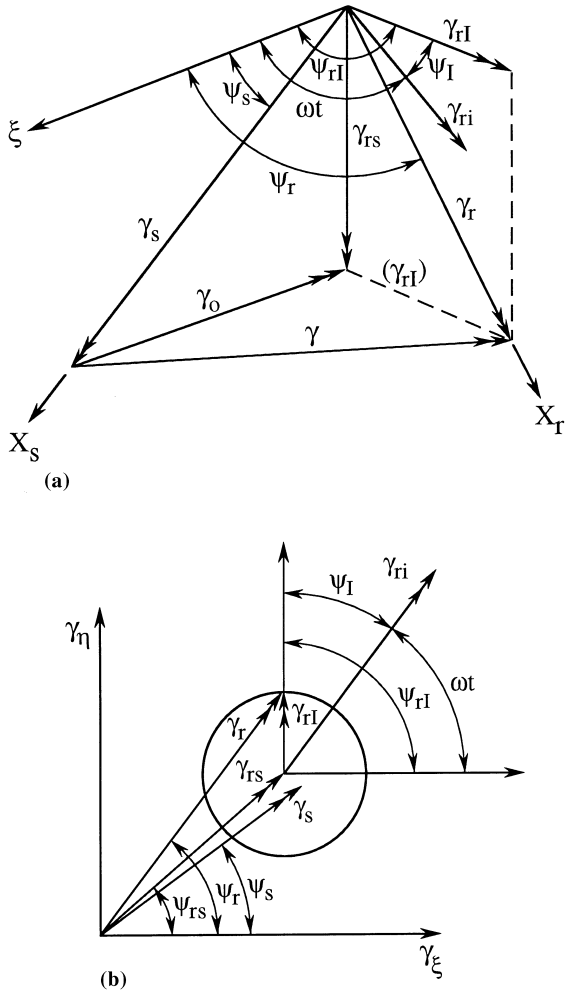

Fig. 2 (a) Vector diagram of tilts and angles and (b) rotor angular response orbit

the rotor initial misalignment, γ_{ri}. Since γ_{rs} is fixed in space, while γ_{rI} rotates at shaft speed, ω, the overall response, γ_r, is a rotating vector with a time varying frequency $\dot{\psi}_r$. The magnitude of both $\dot{\psi}_r$ and γ_r vary cyclically with a constant frequency, ω.

An angular response orbit is introduced to capture the rotor angular dynamic behaviour. It represents the locus of the tip, i.e. the magnitude of the rotor misalignment vector, γ_r, positioned at the instantaneous precession angle, ψ_r (Fig. 2b). The orbit plot is central in the real-time monitoring system described below.

2.2 Dynamic simulation results

First, numerical time integration is performed using the seal parameters from the test rig. The outside seal diameter is 50.8 mm and its inside diameter is 40.6 mm. The O-ring stiffness and damping coefficients are 151.6 N m/rad and 0.0284 N m s/rad, as obtained experimentally in reference [**9**]. The fluid film stiffness and damping coefficients are 3246.3 N m/rad and 58.4 N m s/rad at a clearance of 2 μm, and 717.1 N m/rad and 7.5 N m s/rad at a clearance of 6 μm, as calculated according to reference [**2**]. The sealed water pressure is chosen to be 345 kPa, the shaft speed is set to 28 Hz and the seal coning angle is set to 1 mrad. In the results analysis, special attention is paid to those parameters that characterize the seal dynamics: the rotor misalignment (rotor angular response), the rotor precession angle and the rotor angular response orbit.

The ability of the rotor to track the stator misalignment, γ_s, and stator angle, ψ_s (Fig. 2), is investigated first. The stator misalignment is set of 0.5 mrad. The initial rotor misalignment is arbitrarily set to 1.5 mrad, a value that is different from stator misalignment. This is typical for real seal applications. In reality, the stator angle is fixed, but it can assume any value between 0 and 2π. Therefore, in the simulation the stator angle is checked for different values between 0 and 2π, at $\pi/4$ steps and at 0.2 s intervals and for two different clearances, 2 and 6 μm. The simulation results are plotted in Fig. 3.

It should be noted that the stator angle is fixed in time and the rotor adjusts itself (rotor response) to that fixed stator position. In order to study the steady state rotor response to different stator angles in one computer run, ψ_s is artificially changed at every 0.2 s time interval in the simulation, and the results are plotted as if they are a function of time. Nevertheless, the transients are ignored and only the sections of individual steady state response are studied, detached from both the preceding and the following sections. For example, ψ_r during the time section 0.8–1.0 s in Fig. 3a simply denotes the rotor final steady state precession angle in response to $\psi_s = \pi$ along this arbitrary 0.2 s interval (a heavy line shows clearance of 2 μm and a thin line shows clearance of 6 μm).

It can be seen from Fig. 3a that the rotor can always adapt to any stator angle. The response of the rotor is cyclic about the stator angle, and its amplitude varies with the clearance: the smaller the clearance, the smaller is the amplitude.

Figure 3b shows the rotor misalignment for different stator angles and clearances. The rotor is always capable of adapting itself to the stator misalignment, but its misalignment varies cyclically about that of the stator. The amplitude of the rotor misalignment depends on the clearance but not on the stator angle. The smaller the clearance, the smaller is the amplitude, which is attributed to larger fluid film stiffness and damping coefficients [**2**].

Figure 3c shows the rotor angular response orbit as it changes with various stator angles and two clearances. The simulation starts at the origin, $\gamma_\xi = \gamma_\eta = 0$. The steady state rotor angular response orbit is a circle centred at the point whose polar coordinates are the mean value of the rotor misalignment (the magnitude) and the mean value of rotor precession (the angle). This point, for the parameters investigated here, is close to another point whose polar coordinates are the stator misalignment and the stator angle, ψ_s. The distance

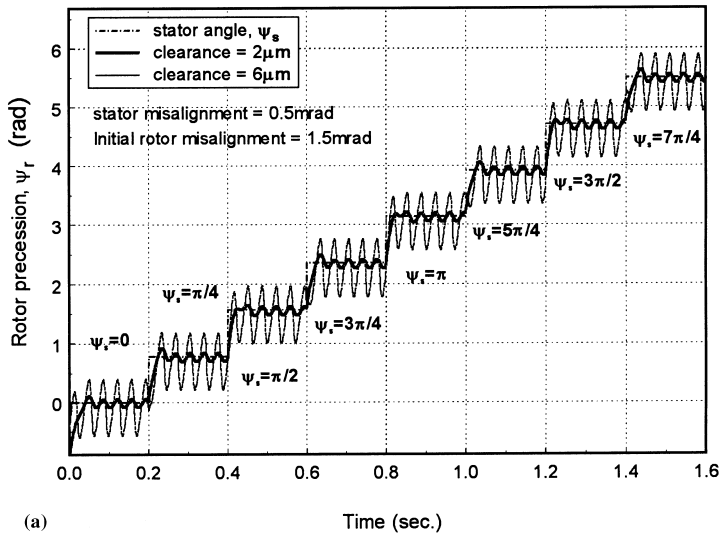

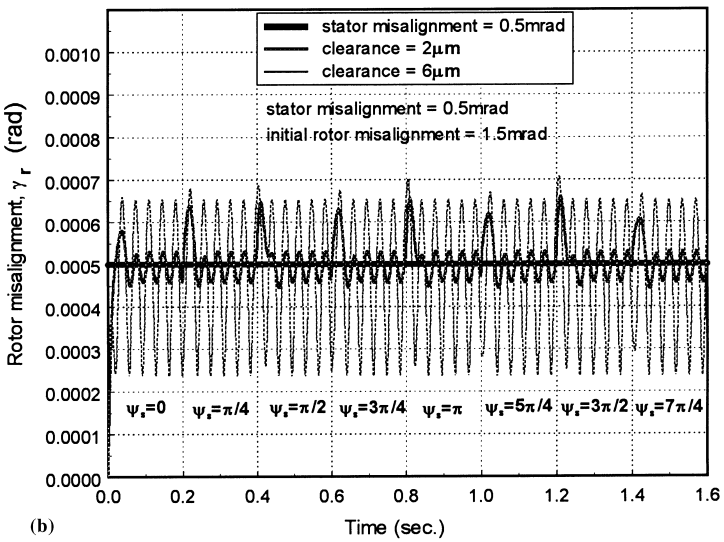

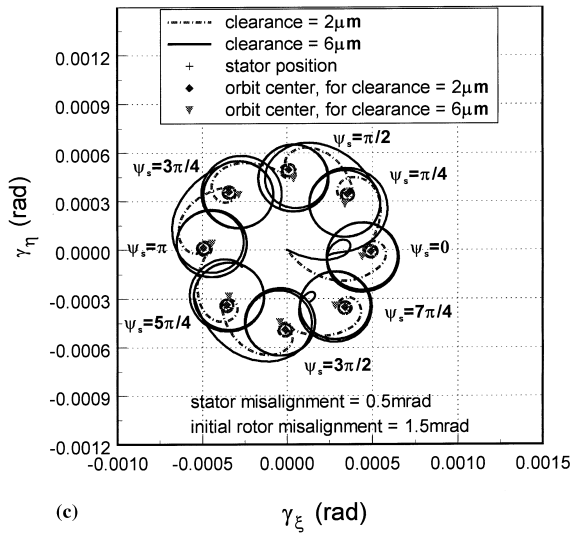

Fig. 3 (a) Simulated rotor precession angle versus time, (b) simulated rotor misalignment versus time for $\gamma_s = 0.5$ mrad and (c) simulated rotor angular response orbits at various stator angles and two seal clearances

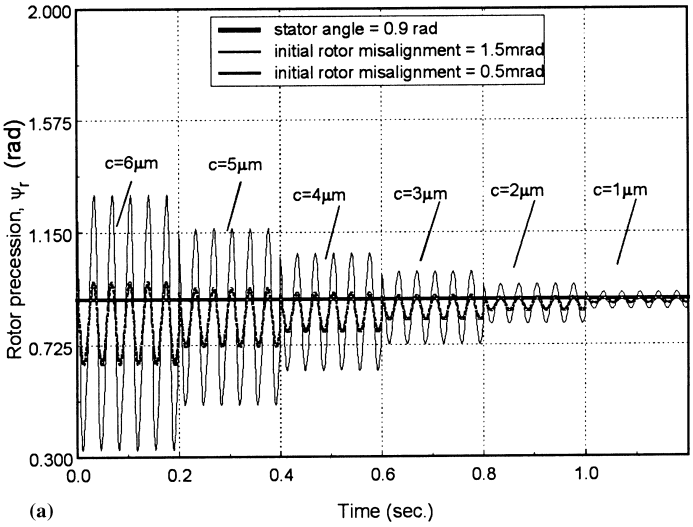

(a)

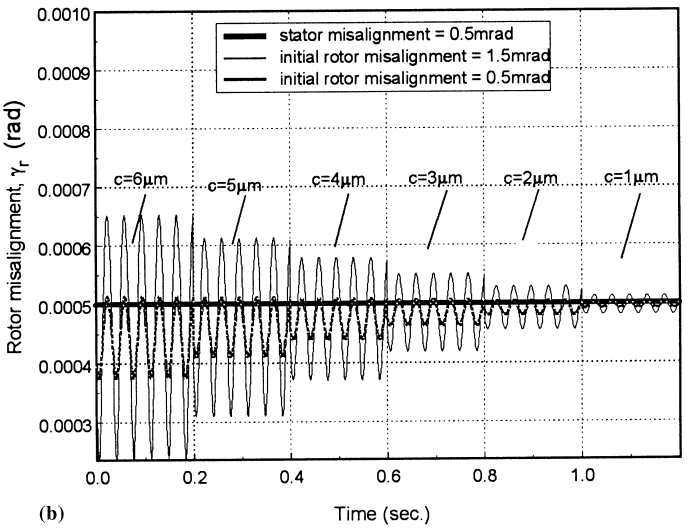

(b)

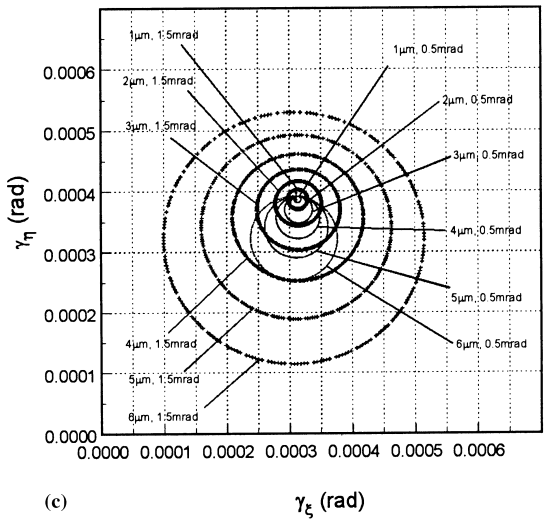

(c)

Fig. 4 (a) Simulated rotor precession angle versus time for changes in seal clearance, (b) simulated rotor misalignment versus time for changes in seal clearance and (c) simulated rotor angular orbit plots for changes in seal clearance (at $\gamma_s = 0.5$ mrad, $\psi_s = 0.9$ rad, $\gamma_{rI} = 0.5$ and 1.5 mrad)

between the two points depends on various seal parameters, such as clearance: the smaller the clearance, the smaller is the distance. The mean value of the rotor misalignment is γ_{rs}. The variation in the rotor misalignment about its mean value is γ_{rI} (Fig. 2).

Because clearance is a very important parameter in seal operation, its effect on rotor response is further investigated. Figures 4a to c show the simulation results for a stator misalignment of $\gamma_s = 0.5$ mrad, while Figs 5a to c show the simulation results for $\gamma_s = 1.5$ mrad. The chosen values of ψ_s for the simulation match those of the experimental results, which follow later. The simulation results are plotted for two different initial rotor misalignments, 0.5 and 1.5 mrad, at six clearances ranging from 1 to 6 μm. The clearance is changed at time intervals of 0.2 s, in a scheme that can be implemented physically in the test rig for the purpose of clearance control [**10**].

It can be seen from Figs 4a and 5a that the ability of the rotor precession angle, ψ_r, to follow the stator angle, ψ_s, varies with clearance. The precession angle better adapts to the stator angle and results in smaller oscillation amplitude as the clearance decreases. The precession angle amplitude also depends on the initial rotor misalignment: the smaller the initial misalignment, the smaller is the amplitude. By comparison it can be seen that, when the stator misalignment is smaller (Fig. 4a), the rotor precession angle tracks the stator angle closer but with a larger amplitude.

Similar conclusions can be drawn from Figs 4b and 5b for the rotor misalignment, γ_r. This misalignment better adjusts itself to the stator corresponding misalignment of $\gamma_s = 0.5$ or 1.5 mrad, when γ_s is smaller. The oscillation amplitudes decrease with the clearance. The amplitudes also depend on the initial rotor misalignment, γ_{ri}: the smaller the initial misalignment, the smaller is the amplitude. Comparison of Figs 4b and 5b also shows that, when the stator misalignment is smaller (Fig. 4b), the rotor misalignment tracks the stator misalignment more closely. The amplitude of the rotor misalignment is essentially the same for both values of stator misalignment.

Figures 4c and 5c show the rotor angular response orbits for the two stator misalignments of 0.5 and 1.5 mrad, respectively, at two different initial rotor misalignments, 0.5 and 1.5 mrad, and six clearances. For both of the initial rotor misalignment cases shown, the radius of the orbit decreases when the clearance decreases. While the loci of orbit centres is not shown in the figures, the results are such that, when the clearance decreases, the centre of the orbit also moves towards the point whose polar coordinates are the stator misalignment and the stator angle. An interesting phenomenon is that, when the initial rotor misalignment is equal to (or close to) the stator misalignment, i.e. $\gamma_{ri} = 0.5$ mrad in Fig. 4c, and $\gamma_{ri} = 1.5$ mrad in Fig. 5c, the rotor response orbits for different clearances pass through a common point. Therefore, for practical monitoring purposes, dynamic responses that pass through the same point indicate that the stator and initial rotor misalignment are close to each other.

3 SEAL DYNAMIC MONITORING

3.1 Seal test rig

The schematic of the non-contacting FMR mechanical face seal test rig is shown in Fig. 1. The rotor is made of AISI 440C stainless steel. It is heat treated and hardened to approximately 56 HRC to increase its surface wear resistance. The rotor end surface is lapped to a flatness of three light bands and polished to a surface roughness of 0.1 μm root mean square (r.m.s.). This rotor is flexibly mounted on a rotating shaft through an elastomer O-ring. This allows the rotor to track the stator misalignment and to move axially. The seal stator assembly is composed of several components: the stator, the spacer and the stator holders. This design is capable of mechanically deforming the stator and producing seals with different coning angles. The stator is a single piece of graphite, whose surface is lapped to a flatness of two light bands and polished to a surface roughness of 0.15 μm (r.m.s.). This stator assembly is fixed in the housing. The shaft is screwed into a spindle driven by a d.c. motor through two timing pulleys and a timing belt. The motor speed is controlled by a speed controller. The housing is made of three parts for convenience in machining, maintenance and adjustment of the test rig. All possible leakage paths are sealed by O-rings.

Pressurized water is supplied from the main water supply line into the housing. Pressurized air is supplied from the main air supply line to the rotor chamber through holes in the housing and the shaft. It is sealed by a lip seal at one end and separated from the water by a contacting seal at the other end. The air pressure can be adjusted manually or by a computer through a voltage-to-pressure (V/P) converter.

The seal operates at an equilibrium position with a certain clearance between the rotor and the stator, where the opening force and closing force are balanced. The opening force is contributed by the hydrostatic and hydrodynamic effects acting in the sealing interface. The hydrostatic force is affected by the seal geometry, coning angle, the seal pressure difference and by the clearance. The contribution of the hydrodynamic effect to the axial force is generally small compared with the hydrostatic force if there is no cavitation and if the seal surface waviness is insignificant. The closing force is composed of the support load contributed by the elastomer O-ring, the hydraulic force acting on the seal and the force, F_{air}, generated by air pressure in the rotor chamber.

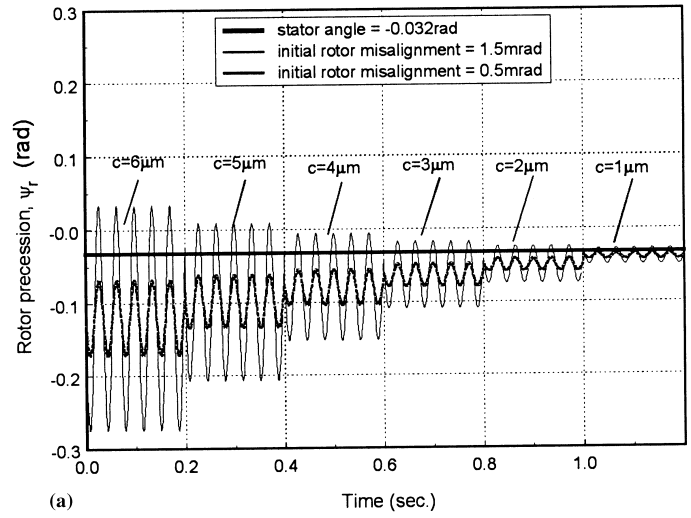

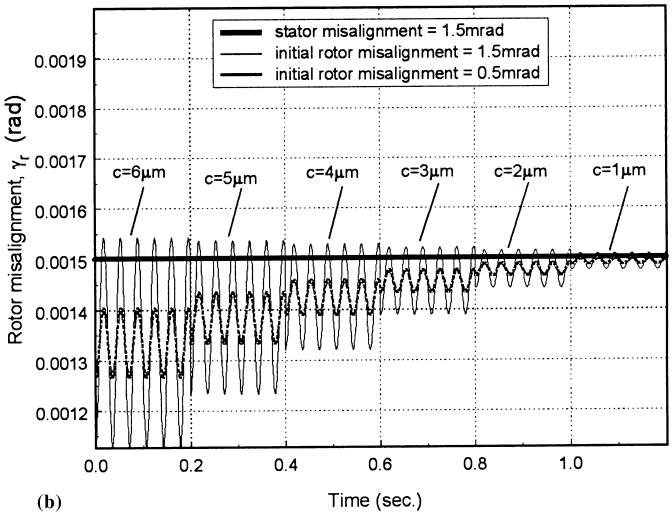

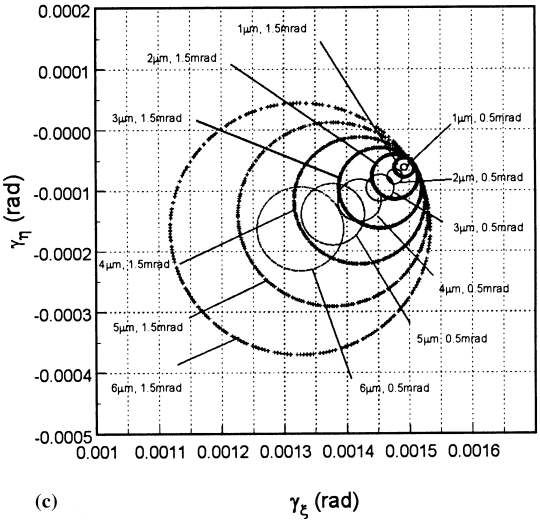

Fig. 5 (a) Simulated rotor precession angle versus time for changes in seal clearance, (b) simulated rotor misalignment versus time for changes in seal clearance and (c) simulated rotor angular orbit plots for changes in seal clearance (at $\gamma_s = 1.5\,\text{mrad}$, $\psi_s = -0.032\,\text{rad}$, $\gamma_{rI} = 0.5$ and $1.5\,\text{mrad}$)

Clearances can be varied by changing the air pressure acting on the back of the rotor in the rotor chamber.

3.2 Monitoring system

Three eddy current proximity probes mounted on the end of the housing are used to detect the instantaneous dynamic response of the rotor. These proximity probes have a bandwidth of about 10 kHz. They can measure the static and dynamic distances between their tips and the rotor end surface. A low-pass filter with a cut-off frequency of 1 kHz is used to eliminate high-frequency cross-talk noises among the probes and also to serve as an anti-aliasing filter. The maximum output of each proximity probe is −24 V. A voltage divider is used to drop the maximum amplified voltages of the proximity probe outputs from −24 to −10 V. The reduced voltages are then sent into a universal board mounted in a personal computer. The board has a floating-point digital signal processor (DSP). The DSP has been supplemented by a set of on-board peripherals, such as analogue-to-digital (A/D) and digital-to-analogue (D/A) converters. The proximity probe signals are obtained through the A/D converter of the board. A flowmeter is also used to measure the leakage of the seal. The proximity probe signals and the leakage measurement are then processed by the on-board DSP and the results are sent to the computer in real-time for on-line display or for data recording. Key dynamic parameters, such as the rotor misalignment, the rotor precession angle, the rotor angular response orbit and the clearance, are monitored. The calculation algorithms for these parameters are described in reference [**11**].

3.3 Experimental and monitoring results

The sealed water pressure is set to 345 kPa, and the shaft speed is set to 28 Hz. The graphite stator in the stator assembly is deformed to provide a coning angle of 1 mrad. The monitored parameters are the same as those in the dynamic simulations, i.e. the rotor misalignment, the rotor precession angle and the rotor angular response orbit. Two sets of experimental results are described in Figs 6 and 7. These are then compared qualitatively with the simulations of Figs 4 and 5 respectively.

The first set of experimental results for four different clearances is presented in Fig. 6. The procedure for taking experimental data is: setting the air pressure in the rotor chamber to 27.6 kPa, running the shaft at 28 Hz and recording the monitored data; repeating this procedure by incrementing the air pressure (by approximately 14 kPa) to 41.4 kPa, then 55.2 kPa and lastly 69.0 kPa. From the leakage measurement (see Fig. 6e) the clearances are calculated to be 6, 2.8, 1.5 and 0.5 μm respectively. Also, from the three proximity probe signals (Fig. 6d) the stator misalignment and angle are calculated to be 0.5 mrad and 0.9 rad respectively. The second set of experimental results is obtained by the same procedure (Fig. 7). This time, however, tests are conducted for six decreasing clearances from 6 to 1 μm, in increments of 1 μm. Again, Fig. 7e depicts the clearances as calculated from the leakage measurement. Figure 7d shows the three proximity probe signals from which the stator misalignment of 1.5 mrad and the stator angle of −0.032 rad (cyclically equivalent to 6.251 rad) are calculated.

As stated, the rotor response is a function of the initial rotor misalignment as well as the stator misalignment [**4**]. The simulations in Section 2 pertain to the four combinations of stator and initial rotor misalignments of 0.5 and 1.5 mrad. The purpose of the physical testing is to verify the seal dynamic behaviour experimentally under similar conditions. However, it should be noted that the initial rotor misalignment is set only once, at the beginning of each set. In the execution of the successive runs for the different clearances, the initial rotor misalignment assumes some value affected by both the previous run and the amount of relaxation present in the two O-rings, which form the flexible rotor support. Therefore, the rotor gradually adjusts itself to the stator misalignment and the initial rotor misalignment is not fixed as theoretically assumed, but varies each time the systems runs and stops (i.e. between clearance changes). Consequently, only the first run in each set of experiments nearly corresponds to the assumed initial rotor misalignment used in the simulation ($\gamma_{rI} = 1.5$ mrad for $C = 6$ μm in Fig. 6 and $\gamma_{rI} = 0.5$ mrad for $C = 6$ μm in Fig. 7). All the other experimental results fit only qualitatively to the simulated ones, exhibiting better dynamic responses because of an effectively decreasing initial rotor misalignment at the beginning of each test. The outcome is smaller final rotor misalignment, displaying tighter rotor response orbits.

Figures 6a and 6b depict, respectively, the changes in the rotor precession angle and the rotor misalignment with the clearance. Both the rotor precession angle and the rotor misalignment vary periodically, and their amplitude decreases as the seal clearance decreases. A similar behaviour is displayed by Figs 4a and b for an initial misalignment of 1.5 mrad. The large peak-to-peak amplitude at the beginning of the operation is due to the large initial rotor misalignment with respect to the stator misalignment (0.5 mrad). As explained, the rotor gradually adjusts itself to the stator misalignment as the clearance decreases and both the rotor precession angle and misalignment amplitudes are also reduced. The mean value of the rotor precession angle approaches the stator angle and the rotor misalignment approaches that of the stator (its behaviour becomes similar to Fig. 4b for an initial rotor misalignment of 0.5 mrad). The same phenomenon is observed by comparing Fig. 6c with Fig. 4c. They show the rotor angular response orbits for

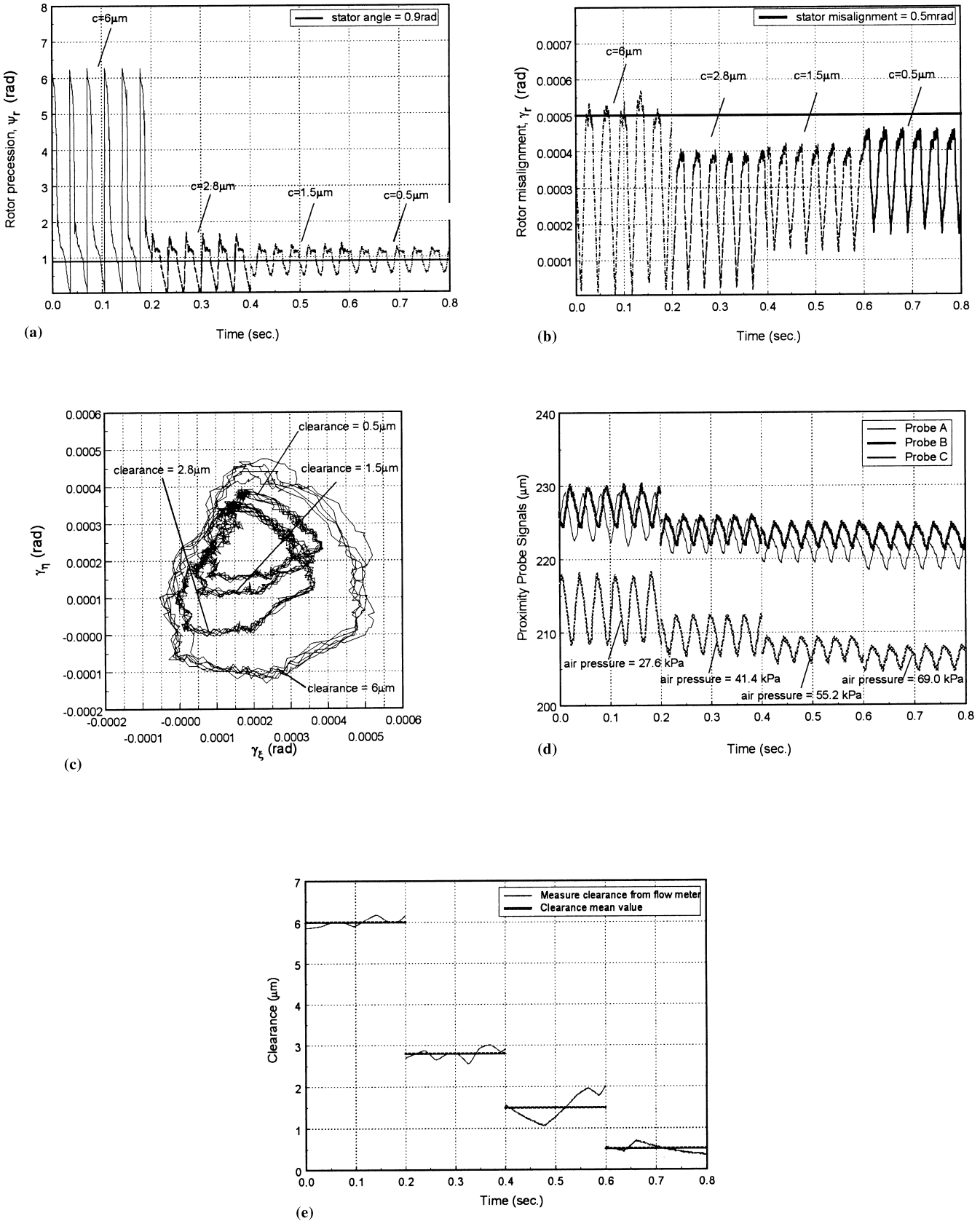

Fig. 6 (a) Experimental rotor precession angle versus time for changes in seal clearance, (b) experimental rotor misalignment versus time for changes in seal clearance, (c) rotor angular misalignment orbit plots for changes in seal clearance, (d) proximity probe signals versus time and (e) seal clearance calculated from flowrate versus time (at $\gamma_s = 0.5$ mrad, $\psi_s = 0.9$ rad)

different clearances in both experiments and in simulation. As expected, the orbits approach circular shapes. The smaller the clearance, the smaller is the orbit size, and the orbit centres approach the point whose polar coordinates are the stator misalignment and the stator angle. At the beginning of the experiment, for clearance of 6 μm, the initial rotor misalignment (presumably 1.5 mrad) is not close to the stator misalignment (0.5 mrad). With the decrease in clearance at the beginning of each test, the initial rotor misalignment decreases as well. Therefore, the experimental orbits (Fig. 6c) are intersecting, having a behaviour between the two extremes of the simulated orbits of Fig. 4c. It should be pointed out that the centre of the orbit has polar coordinates defined by the average of the maximum and minimum of the rotor misalignment and the average of the maximum and minimum of the rotor precession angle. These averages eventually approach the point defined by the stator misalignment and stator angle.

Results obtained from the second set of experiments (Fig. 7) are similar in nature, although the stator and initial rotor misalignments are reversed ($\gamma_s = 1.5$ mrad and $\gamma_{rI} = 0.5$ mrad for $C = 6\,\mu$m). Again, the rotor precession angle is cyclic and its amplitude decreases as the seal clearance decreases (Fig. 7a). This behaviour is qualitatively similar to Fig. 5a for an initial rotor misalignment of 0.5 mrad. Likewise, the rotor misalignment is also periodic and its amplitude decreases as the seal clearance decreases (Fig. 7b). Since its behaviour is similar to that shown in Fig. 5b (for an initial rotor misalignment of 0.5 mrad) the initial rotor misalignment may indeed be about 0.5 mrad and it effectively remains constant between tests (even for smaller clearances). Comparing Figs 7c and 5c shows the resemblance between the experimental orbits and those of the simulation for an initial rotor misalignment of 0.5 mrad. Similarly, the clearances calculated from the proximity probe signals (Fig. 7d) match very well (within a few per cent) with the clearances calculated from the leakage (flowrate) measurements (Fig. 7e).

FFT analyses performed on both experimental sets (Figs 6d and 7d) reveal very minor second higher-harmonic components in the eddy current proximity probe signals for all the tested clearances, indicating that there is no contact between the seal faces [**11**]. Also, the similarity between the experimentally obtained orbits and the numerically simulated orbits (the latter are based upon a non-contacting analytical model) further supports the conclusion that the seal operates in a non-contacting mode.

4 CONCLUSIONS AND RECOMMENDATIONS

Dynamic simulation is performed using the parameters of a non-contacting FMR mechanical face seal test rig. A monitoring system is constructed to monitor the dynamic behaviour of the seal in real time. The similarities between the simulation and monitoring results clearly indicate that the seal dynamic model established by Green [**4**] captured the major dynamic behaviour of the seal. Any subtle differences between the simulation and the monitoring results could have been caused by unavoidable experimental uncertainties, or by the small perturbation assumption made in the development of the analytical model. The fact that the experimental results cover a large range of clearances, which is beyond the small perturbation range, gives more confidence in applying this model to a larger clearance range. The rotor angular misalignment orbit is found to contain information related to the rotor angular response, the rotor precession angle, the stator misalignment and the stator angle.

When a seal operates in non-contacting mode, the seal rotor dynamic behaviour could be better understood by comparing the dynamic monitoring and the simulation results. If contact occurs, the monitored rotor response would be visibly different from the simulated response because the simulation is based upon a non-contacting analytical model. It is expected that the sensors signal will be corrupted by noise and vibration generated by the face contact, and that the misalignment orbit will deviate substantially from the smooth circular one predicted by the simulation for the non-contacting case. Therefore, the monitoring system can potentially function also as a detection system of seal face contact.

A more advanced and proactive step in face seal dynamics is to control the seal rotor dynamic behaviour and prolong its life. A control system that can take meaningful action based on the real-time dynamic monitoring and contact detection results is currently being incorporated [**12**, **13**].

ACKNOWLEDGEMENTS

The authors wish to express their appreciation to the Office of Naval Research for the support of Research Grant N00014-95-1-0539 for Program 'Integrated Diagnostics'. Dr Peter Schmidt serves as Program Officer. The authors also wish to express their appreciation to Mr Andrew Flaherty of Rexnord Corporation for machining the seal rotor and to Mr Laurence Thorwart and Mr David Erich of Pure Carbon Company for providing and machining the graphite stators. This project is also supported in part by a Georgia Tech Foundation Grant, E25-A77, made by Mr Gilbert Bachman. This support is gratefully acknowledged.

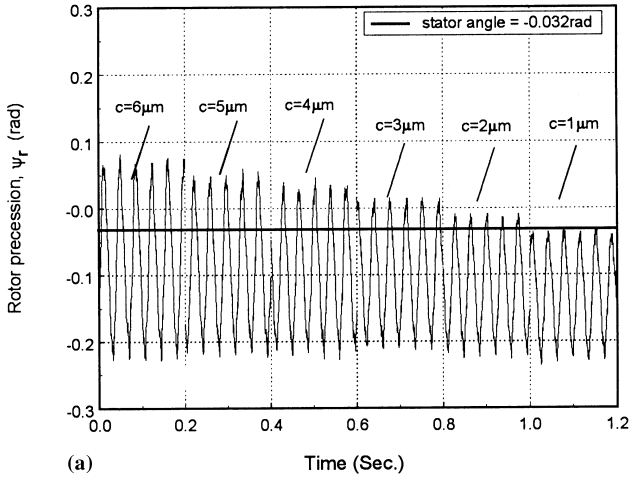

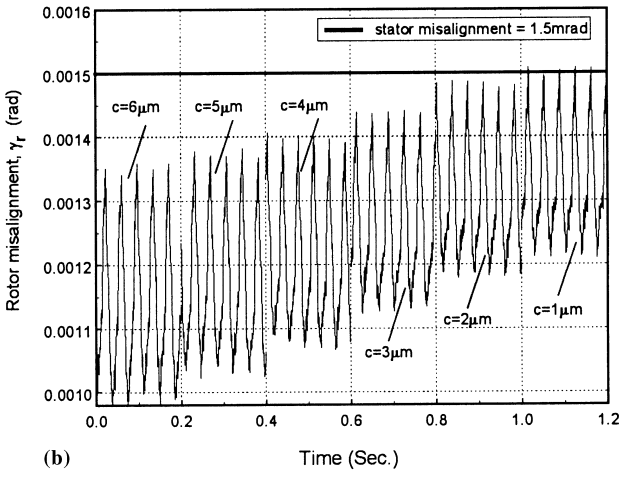

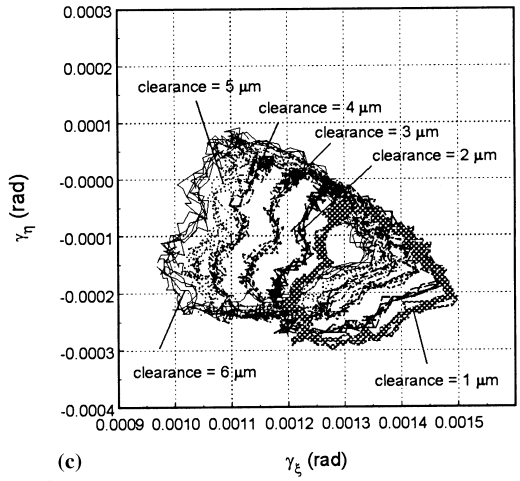

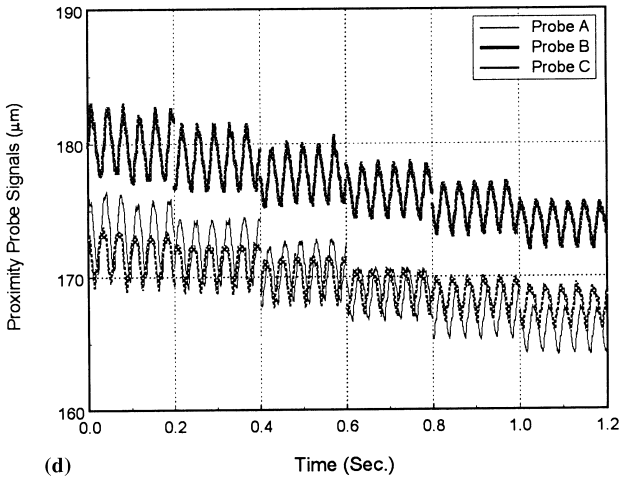

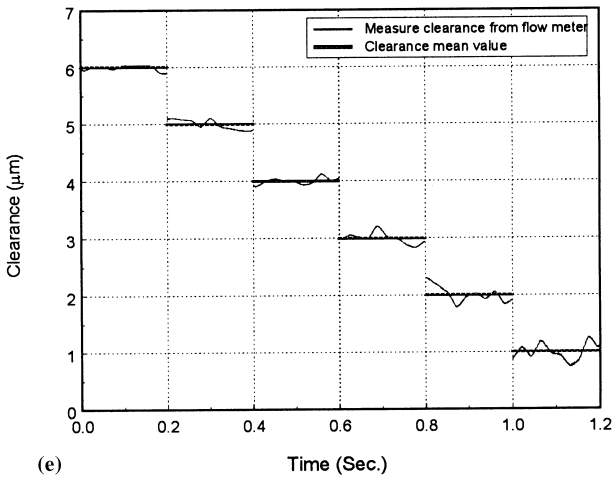

Fig. 7 (a) Experimental rotor precession angle versus time for changes in seal clearance, (b) experimental rotor misalignment versus time for changes in seal clearance, (c) rotor angular misalignment orbit plots for changes in seal clearance (at $\gamma_s = 1.5\,\text{mrad}$, $\psi_s = -0.032\,\text{rad}$, $\gamma_{rI} = 0.5\,\text{mrad}$), (d) proximity probe signals versus time and (e) seal clearance calculated from flowrate versus time (at $\gamma_s = 0.5\,\text{mrad}$, $\psi_s = -0.032\,\text{rad}$)

REFERENCES

1 **Etsion, I.** Mechanical face seal dynamics 1985–1989. *The Shock and Vibr. Dig.*, 1991, **23**(4), 3–7.

2 **Green, I.** The rotor dynamic coefficients of coned-face mechanical seals with inward or outward flow. *Trans. ASME, J. Tribology*, 1987, **109**(1), 129–135.

3 **Green, I.** Gyroscopic and damping effects on the stability of a noncontacting flexibly-mounted rotor mechanical face seal. In Proceedings of 2nd International Symposium on Transport Phenomena, *Dynamics of Rotating Machinery* (Eds J. H. Kim and W.-J. Yang), Hawaii, 1998, 1990, pp. 153–173 (Hemisphere).

4 **Green, I.** Gyroscopic and support effects on the steady-state response of a noncontacting flexibly-mounted rotor mechanical face seal. *Trans. ASME, J. Tribology*, 1989, **111**, 200–208.

5 **Bloch, H. P.** Development and experience with computerized acoustic incipient failure detection (IFD) systems. ASME paper 77-pet-2, 1977.

6 **Kataoka, T., Yamashina, C.** and **Komatsu, M.** Development of an incipient failure detection technique for mechanical seals. In Proceedings of 4th International Pump Symposium, Houston, Texas, 1987, pp. 121–129.

7 **Kennedy, F. E.** and **Grim, J. N.** Observation of contact condition in mechanical face seals. *ASLE Trans.*, 1984, **27**(2), 122–128.

8 **Lee, A. S.** and **Green, I.** Higher harmonic oscillations in a noncontacting FMR mechanical face seal test rig. *Trans. ASME, J. Vibr. and Acoust.*, 1994, **116**(2), 161–167.

9 **Lee, A. S.** An experimental investigation of a noncontacting flexibly mounted rotor mechanical face seal. PhD thesis, Georgia Institute of Technology, 1992.

10 **Zou, M.** and **Green, I.** Clearance control of a mechanical face seal. *STLE Trans.*, 1999, **42**(3), 535–540.

11 **Zou, M.** and **Green, I.** Real-time condition monitoring of mechanical face seal. In Proceedings of 24th Leeds–Lyon Symposium on *Tribology*, Imperial College, London, 1997, pp. 423–430.

12 **Zou, M., Dayan, J.** and **Green, I.** Feasibility of contact elimination of a mechanical face seal through clearance adjustment. ASME Preprint 99-GT-147, *Trans. ASME, J. Engng Gas Turbine and Power*, 1999, **122**(3).

13 **Dayan, J., Zou, M.** and **Green, I.** Contact elimination in mechanical face seals using active control. In Proceedings of 7th IEEE Mediterranean Conference on *Control and Automation*, *MED99*, Haifa, Israel, 28–30 June 1999.

